Influence of surface traction on soft robot undulation

Carmel Majidi[1], Robert F. Shepherd[2], Rebecca K. Kramer[3,4], George M. Whitesides[2,4] and Robert J. Wood[3,4]

Abstract

A pneumatically-driven robot traverses surfaces with different traction by adopting an undulatory mode of locomotion. The robot is composed of soft elastomer (elastic modulus ∼100 kPa), an inextensible but flexible neutral plane, and embedded pneumatic channels. In contrast to conventional robots and wheeled vehicles, the robot deforms elastically to make ground contact over a relatively large area, where interfacial tractions have a unique role in controlling both the speed and direction of locomotion. Here, we demonstrate that for the same undulatory gait, the robot will either move forward or backward depending on the ground composition. Building on mathematical principles of elasticity and friction, we introduce a theoretical model that identifies the tribological properties that determine the direction of locomotion. Though overlooked in the past, this tribology-controlled phenomenon represents a central feature of undulation on smooth, soft, and slippery surfaces. These insights provide a starting point for identifying locomotion strategies that allow soft robots, like their natural invertebrate counterparts, to navigate a broad range of surfaces and terrains.

1. Introduction

Soft robotics represents an exciting new technology that will potentially revolutionize our ability to perform search and rescue operations, assist in human motor tasks, and reduce manufacturing costs. As with natural invertebrates, soft robots are primarily composed of soft materials and fluids, and can elastically deform to reversibly control their shape and functionality. This unique combination of mobility, elastic compliance, and multi-functionality allows soft robots to operate in a broad range of environments and under rapidly changing conditions. Soft robots elastically conform to surfaces and must support interfacial tractions over large areas of their body. In contrast to conventional robots, which are rigid and typically limited to point contacts, the mechanics of soft robots are largely governed by surface interactions and tribology. This is particularly true for locomotion on soft, slippery, muddy, or otherwise mechanically unstable surfaces.

In this manuscript, we examine an extreme case of contact-controlled locomotion in which a soft robot undulates on surfaces that vary in composition, rigidity, and texture. This study helps to identify the relevant physical factors and classical theories that could eventually be used to find locomotion strategies that exploit the robot's unique soft-matter functionalities and allow for versatile navigation on heterogeneous terrain. We performed experiments on a soft, pneumatic robot that was previously introduced by Shepherd et al. (2011). Figure 1 shows the robot executing undulatory locomotion on three different surfaces. The robot is composed of a soft elastomer, an inextensible but flexible neutral plane, and five embedded pneumatic network (pneu-net) actuators. The pneu-net actuators inflate when pressurized with compressed air, causing individual segments of the robot to deflect.

[1]Department of Mechanical Engineering and The Robotics Institute, Carnegie Mellon University, Pittsburgh, Pennsylvania, USA
[2]Department of Chemistry and Chemical Biology, Harvard University, Cambridge, Massachusetts, USA
[3]School of Engineering and Applied Sciences, Harvard University, Cambridge, Massachusetts, USA
[4]Wyss Institute for Biologically Inspired Engineering, Harvard University, Cambridge, Massachusetts, USA

Corresponding author:
Carmel Majidi, Department of Mechanical Engineering and The Robotics Institute, Carnegie Mellon University, 5000 Forbes Avenue, Pittsburgh, Pennsylvania 15213 USA.
Email: cmajidi@andrew.cmu.edu

For the same undulatory pattern, the robot moves forward on felt (Figure 1(a)–(e)), remains stationary on polyethylene (Figure 1(f)–(j)), and moves backwards on wet gelatin (Figure 1(k)–(o)). We predict these differences in trajectory with a comprehensive theoretical model that couples ground interactions and pneumatic inflation with the elastic deformation and undulatory locomotion of the soft robot. By identifying the governing relationship between gait, contact, and trajectory, we can tune the actuation of the robot in response to the anticipated ground conditions. Moreover, these theoretical relationships may eventually contribute to generalized models that aid in deterministic motion planning by simulating locomotion on a broad range of surfaces that typically arise in field exploration, disaster recovery, and medicine.

For wet and non-rigid surfaces like mud or soft sand, a flat, soft-bodied robot with an undulatory gait yields a large area of contact and reduces interfacial pressure between the robot and surface, relative to walking or crawling. Area-controlled contributions to interfacial mechanics also influence the undulatory locomotion of natural invertebrates such as earthworms (Garrey and Moore, 1915), nereidid polychaetes (Gray, 1939), larval diptera (Berrigan and Pepin, 1995), and caterpillars (Casey, 1991). For example, Shen et al. (2012) have recently shown that the undulation of nematodes on soft agar gels are strongly influenced by surface drag. Similarly, Maladen et al. (2009) demonstrate that sandfish lizards undulating through dry sand appear to swim with a speed that is controlled by thrust and drag produced by the frictional grain flow of the surrounding media. A theoretical study of snake locomotion on a smooth, rigid halfspace show that even in the absence of fluidic drag, interfacial forces generated by Coulomb friction can have a significant influence on the shape of the snake as it undulates (Guo and Mahadevan, 2008). Other friction-controlled locomotion strategies where interfacial mechanics have a central role include two-anchor crawling and peristalsis (Alexandar, 2003).

Like its biological counterparts, the soft robot is lightweight and will not sink into soft surfaces as a heavier conventional robot would. As with other recent efforts by Ilievski et al. (2011) and Morin et al. (2012), each segment of the soft robot is powered with pneu-net actuators that reversibly control both the natural curvature and flexural rigidity of the robot's limbs and torso. This paradigm in soft robotic actuation builds on previous work by Suzumori et al. (1991, 2007) as well as recent advancements in soft microfluidics fabrication through rapid prototyping and soft lithography (Xia and Whitesides, 1998; Qin, Xia and Whitesides, 2010; Quake and Scherer, 2000). Other approaches to soft robotic actuation include shape memory alloys (Seok et al., 2010; Lin, Leisk and Trimmer, 2011), dielectric elastomers (Cianchetti et al., 2009), ionic-polymer-metal composites (Arena et al., 2006; Yeom and Oh, 2009), and natural muscle tissue (Feinberg et al., 2007; Nawroth et al., 2012).

2. Principles of operation

The quadruped robot is composed of a soft silicone elastomer (Ecoflex^{TM} 0030; Smooth-On, Inc.) embedded with five pneu-net actuators located in the torso and four limbs (Shepherd et al., 2011). The bottom of the robot is covered with an inextensible, strain-limiting layer that corresponds to the neutral plane of bending. Pneumatic actuation is coordinated so that the front and back pair of limbs are simultaneously inflated to produce an out-of-plane undulatory motion. The direction and step size of each undulatory sequence is governed by the pressure-controlled curvature and flexural rigidity of the inflated segments as well as the load- and adhesion-controlled friction between the elastomer and substrate.

2.1. Pneu-net curvature and rigidity

Just as with McKibben air muscles and other mechanisms for pneumatic and hydraulic actuation, pneu-net actuators exhibit changes in both natural bending curvature and flexural rigidity. When compressed air with a pressure p is delivered to the pneu-net, the embedded air chambers inflate and cause the surrounding elastomer to bend from a naturally flat configuration to a naturally curved shape with curvature $\kappa_p = \kappa_p(p)$. In addition to bending, the compressed air increases the flexural rigidity of the elastomer from an original value of D_0 governed by the elastic rigidity of the elastomer to a new value $D_p = D_p(p)$ that also includes the resistance of compressed air to changes in chamber volume.

We use the principle of minimum potential energy to estimate the coupling between bending curvature κ_p and flexural rigidity D_p of a single inflated segment. We parameterize the deformation of a single pneu-net air chamber by the curvature κ of the neutral bending plane. Geometrically, this curvature corresponds to a bending radius $R = 1/\kappa$, which is defined in Figure 2 along with the height H and width c of the air chamber and arclength x and thickness t of the neutral bending plane. Both the air chamber and strain-limiting layer have a depth w into the page.

In the absence of an external bending moment M, the total potential energy stored in the air chamber and surrounding elastomer is calculated as

$$\Pi = \frac{1}{2}D\kappa^2 x \quad pV \tag{1}$$

Here, $D = Ewt^3/12$ is the flexural rigidity of the strain-limiting layer, E is its elastic (Young's) modulus, and V is the volume of compressed air. Ignoring the thickness of the strain-limiting layer, V is approximately

$$V \quad \frac{1}{2}\psi \left\{ (R + H)^2 \quad R^2 \right\} w \tag{2}$$

where, referring to Figure 2(c), $\psi = c/R = \kappa c$ is the angle of the arclength c along the strain-limiting layer. For static equilibrium, Π must be stationary with respect to κ, i.e.
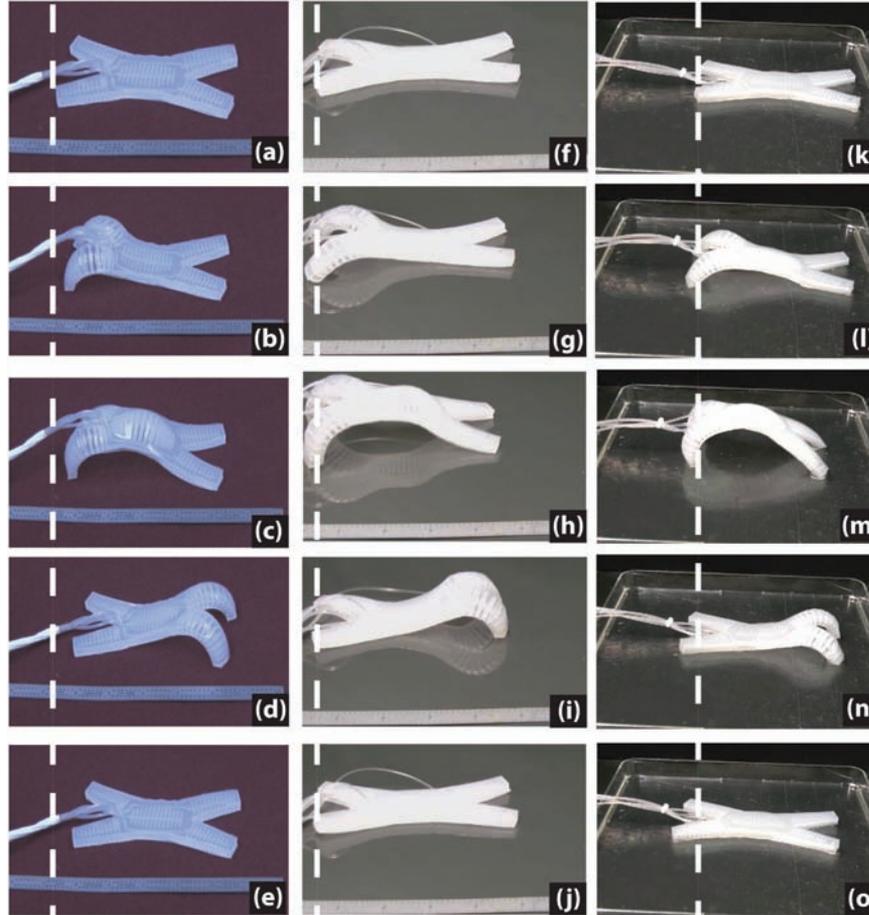
Fig. 1. Pneumatically-actuated, soft, quadruped robot executing an undulatory gait. The composition of the surface influences the direction of motion for the same undulatory pattern: (a)–(e) left to right on felt, (f)–(j) no displacement on polyethylene, (k)–(o) right to left on wet gelatin.

$\partial \Pi / \partial \kappa = 0$. Substituting the expressions for D, V, and ψ into equation (1) and solving $\partial \Pi / \partial \kappa = 0$ for κ yields

$$\kappa_p = \frac{6pH^2c}{Et^3x} \qquad (3)$$

This corresponds to the new bending curvature when the air chambers have a prescribed internal pressure p.

In addition to changing the bending curvature, filling the chambers with compressed air also increases the flexural rigidity of the pneu-net actuator. In the absence of compressed air, the flexural rigidity is approximately equal to the rigidity of the strain-limiting layer, i.e. $D_0 \quad D$. When pressurized, the flexural rigidity increases to $D_p = D_p(p)$, which is determined by calculating the change in curvature $\Delta \kappa = \kappa \quad \kappa_p$ induced by an externally applied bending moment M. By definition

$$D_p = \lim_{M \to 0} \frac{M}{\kappa \quad \kappa_p} \qquad (4)$$

where κ_p is obtained from equation (3). The final curvature κ is again determined by solving the equilibrium condition

$\partial \Pi / \partial \kappa = 0$. However, now the expression for potential energy must incorporate the contribution of the external bending moment as well as the compressibility of the pressurized air that is sealed inside of the pneu-net chambers. This analysis assumes that once inflated, the pneumatic valves are closed and the sealed air obeys the ideal gas law: $p_f V = p V_p$. Here, p is the prescribed pressure that leads to the curvature κ_p in the absence of bending moment, calculated in equation (3), and V_p is the corresponding air chamber volume

$$V_p = \frac{1}{2} c \kappa_p \left\{ \left(\kappa_p^{\;1} + H \right)^2 \quad \kappa_p^{\;2} \right\} w \qquad (5)$$

When a moment is applied, the actuator bends to a final curvature κ, which leads to a new enclosed volume V and a final pressure $p_f = p V_p / V$. The final curvature is determined by minimizing the following potential energy

$$\Pi = \frac{1}{2} D \kappa^2 x \quad p V_p \ln \left(\frac{V}{V_p} \right) \quad M \kappa x \qquad (6)$$
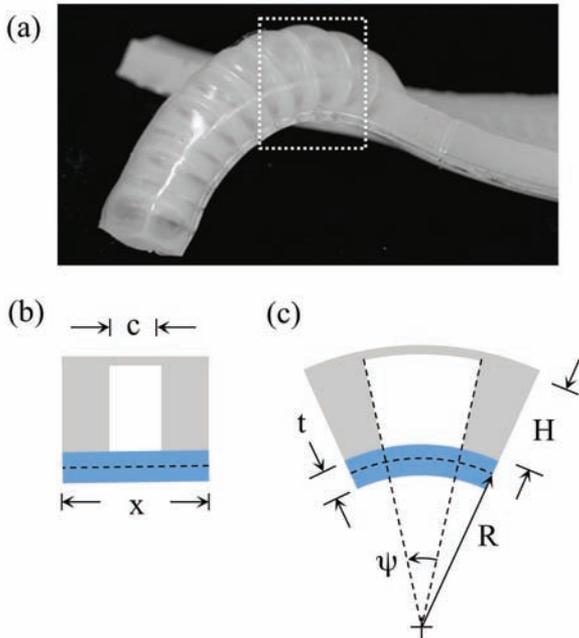
Fig. 2. (a) Inflated pneu-net chambers in the limb of a soft quadruped (Shepherd et al., 2011). Pneu-net chamber (b) before and (c) after inflation.

where the expression for V is presented in equation (2). Solving $\partial \Pi / \partial \kappa = 0$ for κ and performing a Taylor expansion about $M = 0$ yields

$$\kappa \quad \kappa_p + \frac{6M}{w}\left\{\frac{1}{Et^3} + \frac{x}{6cH^3p + Et^3x}\right\} + O\left[M^2\right] \quad (7)$$

This implies

$$D_p = \lim_{M \to 0} \frac{M}{\kappa \quad \kappa_p} = \frac{Ewt^3(6cH6^3p + Et^3x)}{12(3cH^3p + Et^3x)} \quad (8)$$

Next, performing a Taylor expansion about $p = 0$ implies that for small and moderate pressures

$$D_p \quad D + \left\{\frac{cH^3w}{4x}\right\}p \quad (9)$$

In summary, curvature and flexural rigidity have linear and affine dependencies on pressure, respectively. That is $\kappa_p = \alpha p$ and $D_p \quad D + \eta p$, where the fixed constants $\alpha = 6H^2c/Et^3x, D = Ewt^3/12$ and $\eta = cH^3w/4x$ are based on the pneu-net design.

2.2. Friction model

We use Coulomb's law to estimate the sliding friction between the robot and the ground. This parameterization is composed of a load- and area-controlled term, V_t and V_s, respectively (Yoshizawa et al. 1993). The load-controlled term is simply proportional to the vertical component N

of the reaction force and corresponds to Amonton's classical law $V_t = \mu N$, where μ is the coefficient of friction. The area-controlled term scales with the area A of contact: $V_s = \tau A$, where the interfacial shear strength τ is a fixed constant that is mostly governed by adhesion or mechanical interlocking between the contacting surfaces.

Referring to the undulatory sequence in Figure 1(c), the soft robot only makes ground contact at its two ends, which are separated by a horizontal distance Λ. As shown in the figure, each end may either make point contact with the ground or flatten to make "side contact" over a finite length λ. For an end that is in point contact, the maximum shear force that the interface can support is assumed to be equal to V_t. For side contact, the interface has a maximum sliding resistance of $V_s = \tau A$, where $A = q\lambda$ and q is the total width of the robot.

For each incremental change in the pressures p_i, the displacement of the soft robot is determined by the change in the horizontal separation Λ between the two ends. In general, Λ will be different than the value computed in the previous time step. Therefore, in order to accommodate the current deformation, one or both ends of the robot must slide. We assume that the end with the larger sliding resistance remains anchored while the opposite end slides to accommodate the total change in distance between the two ends of the robot. When both ends have the same sliding resistance (for example, when the robot only engages in tip contact), the two ends are assumed to slide an equal distance in opposite directions.

In order to model locomotion on felt and wet gelatin, we examine the two extreme conditions $\{V_t = 0, \tau = 1\}$ and $\{V_t = 1, \tau = 0\}$. The first condition is appropriate for a non-slippery surface like felt, in which sliding resistance scales with the area of contact. In this case, the robot will anchor itself along the length of side contact and pull in or push out the actuated segment. Alternatively, for slippery surfaces like wet gelatin, the second tribological condition is more appropriate. In this case, the area of side contact is free to slide and is dragged along by the point contact, which digs into the surface and functions as an anchor. Lastly, for locomotion on polyethylene, we assume that the interface has frictional resistance to both tip and side contact and let $\{V_t = 0.5, \tau = 1\}$.

2.3. Method for modeling locomotion

Let the indices $i = 1, 2$, and 3, correspond to the left, middle, and right segments, respectively. When compressed air is delivered to the ith segment, the segment will inflate on one side and bend so that the neutral plane has a natural bending curvature $\kappa_i = \alpha p_i$ and flexural rigidity $D_i = D_0 + \eta p_i$. In addition to internal stress from the pressurized air, each segment is also subject to a gravitational load w as well as internal forces and moments transferred by the attached segments. Together, these loads cause the pressurized segment to deflect elastically from the surface by
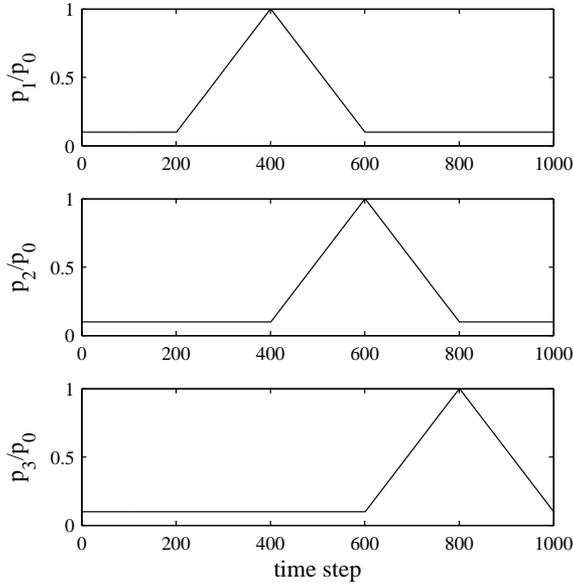
Fig. 3. Simulated and experimental actuation sequence for segments $i = 1, 2, 3$.

a vertical distance y_i that varies along the arclength s. We determine the algebraic expression $y_i = y_i(s)$ by solving the balance laws and boundary conditions in elastic rod theory for static equilibrium (see Appendix A for more details).

Assuming moderate deflections, the slope of each segment and its cosine are approximated as $y_i = dy_i/ds$ and $1 - (y_i)^2/2$, respectively. Therefore, the two ends are separated by a distance

$$\Lambda = \int_0^{L_1} \left\{ 1 - \frac{1}{2}(y_1)^2 \right\} ds + \int_{L_1}^{L_1+L_2} \left\{ 1 - \frac{1}{2}(y_2)^2 \right\} ds$$
$$+ \int_{L_1+L_2}^{L} \left\{ 1 - \frac{1}{2}(y_3)^2 \right\} ds. \tag{10}$$

Here, L_i corresponds to the length of the ith segment and $L = L_1 + L_2 + L_3$. Solutions for y_i are also used to estimate the length λ along which each end of the robot makes contact with the ground. As discussed in the previous section, this is used to calculate the interfacial sliding resistance and determine which end will slide in order to accommodate changes in Λ at each time step.

We use Matlab R2009b (The Mathworks, Inc.) to calculate and render the shape and displacement of the robot for the sequence of pressures presented in Figure 3. The simulation is quasi-static and the time steps correspond to incremental changes in pressure. With this simulation, we observe the gait of the soft robot over several undulatory cycles and calculate the total lateral displacement Δ of the robot's leading end. This simulation also allows us to identify the peak values for p_i and corresponding amplitude of undulation that maximize Δ over a complete cycle.

3. Experimental method

We produce the robot by casting silicone elastomer (EcoFlex 0030; Smooth-On, Inc.) in a three-dimensional (3D), printed mold (Dimension Elite; Stratasys, Inc.) and then sealing the casted features with a layer of additional elastomer and a relatively inextensible thin film of poly(dimethylsiloxane) (PDMS) (Sylgard 184; Dow-Corning) (Shepherd et al, 2011; Ilievski et al, 2011). Flexible pneumatic tubes deliver compressed air to each pneu-net actuator. Air pressure is computer-controlled with independently operated solenoid valves.

To achieve an undulatory gait, the three segments of the robot are pressurized in succession from rear to front with 7 psi (0.5 atm) of pressure. Each segment is pressurized and depressurized with the same sequence that is implemented in the simulation (Figure 3). Shepherd et al. (2011) previously used a similar sequence to actuate a soft, quadruped robot for undulatory locomotion on a rigid, flat surface.

Experiments are performed on flat substrates composed of felt, polyethylene, and hydrated gelatin. For each of the three substrates, the robot executes the same sequence of undulatory motions. We record the motion using a video camera and compare the relative position of the robot with predictions obtained from theory at each stage of the actuation sequence. Using this technique, we can establish the displacement Δ and direction of travel after one undulatory cycle.

4. Results and discussion

We performed the theoretical simulation for $\{V_t = 0, \tau = 1\}$, $\{V_t = 0.5, \tau = 1\}$, and $\{V_t = 1, \tau = 0\}$ in order to model locomotion on felt, polyethylene, and wet gelatin, respectively. In each simulation, the segments were actuated in a staggered manner (Figure 3) that heuristically simulates the two-anchor strategy for inchworm locomotion. The phase lag between each segment introduces a temporal asymmetry that allows the robot to translate by a finite amount by the end of the undulatory cycle. We observed that the direction of this motion depends on the relative magnitude of the coefficients V_t and τ.

Figure 4 presents the theoretical and experimental results for locomotion on all three surfaces. The black and grey lines correspond to the uninflated (passive) and inflated (activated) segments, respectively. For locomotion on felt $\{V_t = 0, \tau = 1\}$, the robot will anchor itself along the length of side contact and move from left to right, as shown in Figure 4(a). Physically, this friction law implies that interfacial shear strength is strongly influenced by contact area rather than pressure. On polyethylene, $\{V_t = 0.5, \tau = 1\}$ and friction is governed by a combination of side and tip contact. As segment 1 inflates, the left end of the robot makes tip contact and initially slides to the right. However, as the length of side contact in segments 2 and 3 decreases, the friction at the tip V_t eventually exceeds V_s and the robot
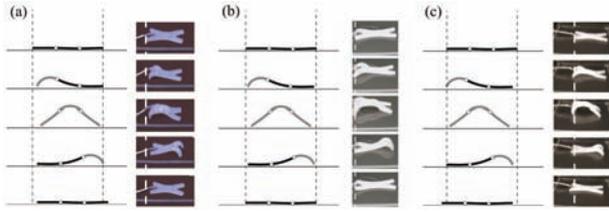
Fig. 4. Simulated and experimental locomotion of soft robot on (a) felt, (b) polyethylene, and (c) wet gelatin using the actuation sequence in Figure 3. On felt, friction scales with contact area and the robot is anchored by the end that is flat against the surface. On polyethylene, friction is alternately governed by tip and side contact, resulting in zero net displacement. On wet gelatin, the surface is slippery and the robot anchors itself at the point contact, where the end digs into the substrate. The black and grey lines correspond to the uninflated (passive) and inflated (activated) segments, respectively.
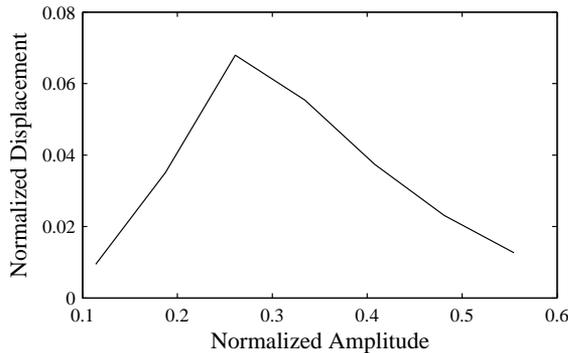

Fig. 5. Theoretical prediction for the maximum amplitude versus final displacement after a single undulatory cycle on felt or gelatin. Normalized with respect to the total length of the robot.

becomes anchored at its left end. During the complete undulatory cycle, the tip and side contacts alternate as kinematic anchors and we observe no net displacement (Figure 4(b)). Lastly, for locomotion on gelatin, the area of side contact is free to slide $\{V_t = 1, \tau = 0\}$. In this case, the robot will be anchored at the tip contact and move to the left, as shown in Figure 4(c). This case corresponds to an interfacial shear strength that is controlled by static friction and depends on pressure rather than area. In practice, this occurs when the robot is able to dig into a soft and deformable surface.

As shown in Figure 5, our simulation predicts that displacement on felt or gelatin is greatest when the undulatory amplitude is approximately 25% of the robot's length. When the amplitude is less than this, the separation Λ remains close to the natural length of the robot and the relative displacement of the two ends at each time step will be negligible. When the amplitude is much larger than this optimal value, both ends of the robot remain in point contact over most of the undulatory cycle and hence slide toward or away from each other by the same amount.

Undulation results in relatively low contact pressures on the ground, since the weight of the robot is distributed over a large area relative to legged robots. This property enables the robot to traverse soft and slippery surfaces like hydrated gelatin. However, as demonstrated by the theory and experiments, the tribological properties of the surface will govern the order in which the pneu-net actuators need to be activated for forward motion. In order to traverse heterogeneous terrain, the robot must alter its undulatory gait in order to adapt to variations in surface traction and rigidity. For example, if the robot undulates from a non-slippery ("felt-like"; $V_t = 0, \tau = 1$) to a soft and slippery ("wet gelatin-like"; $V_t = 1, \tau = 0$) surface, then it will have to reverse its actuation sequence (i.e. from 1   2   3 to 3   2   1) in order to maintain forward motion.

The theoretical model is based on linear beam theory, Coulomb's friction law, and a simplified energy analysis to estimate the dependency of bending curvature and flexural rigidity on air pressure. This model accurately predicts the direction of undulatory motion but has not been tested to establish its accuracy in predicting step size and out-of-plane deflection. In order to make detailed predictions of the robot's elastic deformation, we must revise the theory to more accurately model ground contact and pneu-net inflation. For point contacts, the theory should include the influence of tip angle on sliding friction.

In order to more accurately predict $\kappa_p = \kappa_p(p)$ and $D_p = D_p(p)$, we must relax the assumption that the sealing membrane deflects into an arc and instead treat its curvature as an additional unknown variable that minimizes potential energy. For large deflections, we should also relax the assumption of linear beam deformation and solve $y_i = y_i(s)$ numerically with finite differencing methods. This modified theory for bending curvature and flexural rigidity can be validated by comparison with results obtained from experimental measurement and finite element simulation. However, although relaxing these simplifying assumptions will make the theory more accurate, it will eliminate the algebraic form of the solutions for κ_p, D_p, and y_i and significantly slow the simulation speed. For the current purpose of examining the influence of surface traction, the simplified theory is adequate in capturing the primary physical factors that govern locomotion.

This work demonstrates that tribological conditions at the interface between the robot and ground can have a dramatic impact on locomotion. Understanding the relationship between ground friction and locomotion is important for developing simulation tools that will eventually inform strategies for deterministic motion planning in environments that have a variety of surface conditions. However, deterministic motion planning is challenging when surface conditions are not known, rapidly changing, or highly heterogeneous (with length scales at or below the body length of the robot). In these "noisy" environments, the control strategy must incorporate sensing, feedback, and more robust models that account for dynamic and mixed

surface conditions. Alternatively, the robot may have to adopt alternative locomotion strategies such as walking or crawling, which have previously been demonstrated for the quadruped by Shepherd et al. (2011). These are especially necessary for surfaces (like the polyethylene substrate in Figure 4(b); $V_t = 0.5, \tau = 1$) on which the soft robot cannot achieve the tractions required for forward undulation.

Also, the theory and experiments are limited to smooth, flat surfaces that can be modeled with Coulomb's friction law. However, during field exploration, the robot may encounter viscous or granular surfaces, such as oil slicks, mud, and sand, which cannot be accurately modeled with the theory in section 2.2. Instead, we will have to adopt a tribological model that incorporates boundary lubrication, hydrodynamic lubrication, or other modes of fluidic friction and drag (Persson, 2000; Maladen et al., 2009). In addition to fluidic and viscoelastic effects, the surface may be sticky and require significant peel force to detach robot segments that are in side contact. Adhesion requires a modified theory that addresses the influence of peel resistance and adhesion-controlled stability on the elastic deformation of the robot (Majidi et al., 2012).

5. Conclusion

In summary, we have shown that the interfacial shear strength and coefficient of friction of the surface on which our soft robot undulates determines the direction of locomotion. A predictive theoretical model based on friction laws for a soft, undulating sheet has been presented. This model may be implemented in order to control the motion and maximize displacement of a soft, undulating robot along a prescribed direction. In general, to drive the robot on soft and slippery surfaces, pressurizing the segments from back to front will move the robot forward and pressurizing the segments from front to back will move the robot backwards. In contrast, for higher traction surfaces, forward motion requires actuation from back to front.

Future efforts will focus on more generalized modeling methods that predict motion for a broader range of robot designs, gaits, and surface conditions. These include crawling and rolling on flat and inclined surfaces and robots with more than three body segments or multiple limbs that are capable of turning and lateral motion. As in the present analysis, these models must account for the governing role of contact mechanics and friction on elastic deformation and trajectory. We also plan to improve the theory for a single pneu-net actuator and perform experimental validation along with comparisons to the results of finite element analysis. Lastly, experimental validation of the prediction in Figure 5 for optimal undulatory amplitude would provide further evidence of the theory that locomotion is governed by the competition between friction from tip and side contact.

References

Alexandar RM (2003) *Principles of Animal Locomotion*. Princeton: Princeton University Press, pp. 86–89.

Arena P, Bonomo C, Fortuna L et al. (2006) Design and control of an IPMC wormlike robot. *IEEE Transactions on Systems, Man, and Cybernetics, Part B: Cybernetics* 36(5): 1044–1052.

Berrigan D and Pepin DJ (1995) How maggots move – allometry and kinematics of crawling in larval diptera. *Journal of Insect Physiology* 41(4): 329–337.

Casey TM (1991) Energetics of caterpillar loco-motion – biomechanical constraints of a hydraulic skeleton. *Science* 252(5002): 112–114.

Cianchetti M, Mattoli V, Mazzolai B et al. (2009) A new design methodology of electrstrictive actuators for bio-inspired robotics. *Sensors and Actuators B* 142(1): 288–297.

Feinberg AW, Feigel A, Shevkoplyas SS et al. (2007) Muscular thin films for building actuators and powering devices. *Science* 317(5843): 1366–1370.

Garrey WE and Moore AR (1915) Peristalsis and coordination in the earthworm. *American Journal of Physiology* 39(2): 139–148.

Gray J (1939) Studies in animal locomotion VIII. The kinetics of locomotion of Nereis diversicolor. *Journal of Experimental Biology* 16(1): 9–17.

Guo ZV and Mahadevan L (2008) Limbless undulatory propulsion on land. *Proceedings of the National Academy of Sciences USA (PNAS)* 105: 3179–3184.

Ilievski F, Mazzeo AD, Shepherd RF et al. (2011) Soft robotics for chemists. *Angewandte Chemie* 123(8): 1930–1935.

Lin HT, Leisk GG and Trimmer B (2011) GoQBot: a caterpillar-inspired soft-bodied rolling robot. *Bioinspiration and Biomimetics* 6(2): 026007.

Majidi C, O'Reilly OM and Williams JA (2012) On the stability of a rod adhering to a rigid surface: shear-induced stable adhesion and the instability of peeling. *Journal of Mechanics and Physics of Solids* 60: 827–843.

Maladen RD, Ding Y, Li C et al. (2009) Undulatory swimming in sand: subsurface locomotion of the sandfish lizard. *Science* 325: 314–318.

Morin SA, Shepherd RF, Kwok SW et al. (2012) Camouflage and display for soft machines. *Science* 337(6096): 828–832.

Nawroth JC, Lee H, Feinberg AW et al. (2012) A tissue-engineered jellyfish with biomimetic propulsion. *Nature Biotechnology* 30(8): 792–797.

Persson BNJ (2000) *Sliding Friction: Physical Principles and Applications*. Berlin: Springer, pp. 101–161.

Qin D, Xia Y and Whitesides GM (2010) Soft lithography for micro- and nanoscale patterning. *Nature Protocols* 5(3): 491–502.

Quake SR and Scherer A. (2000) From micro- to nanofabrication with soft materials. *Science* 290(5496): 1536–1540.

Seok S, Onal CD, Wood R et al. (2010) Peristaltic locomotion with antagonistic actuators in soft robotics. In: *IEEE international conference on robotics and automation (ICRA)*, Anchorage, Alaska, USA, 3–8 May 2010, pp. 1228–1233.

Shen XN, Sznitman J, Krajacic P et al. (2012) Undulatory loco-
    motion of Caenorhabditis elegans on wet surfaces. *Biophysical
    Journal* 102: 2772–2781.
Shepherd RF, Ilievski F, Choi W et al. (2011) Multigait soft
    robot. *Proceedings of the National Academy of Sciences USA*
    108(51): 20400–20403.
Suzumori K, Iikura S and Tanaka H. (1991) Development of
    flexible microactuator and its applications to robotic mech-
    anisms. In: *IEEE international conference on robotics and
    automation (ICRA)*, Sacramento, California, USA, April 1991,
    pp. 1622–1627.
Suzumori K, Endo S, Kanda T et al. (2007) A bending pneumatic
    rubber actuator realizing soft-bodied manta swimming robot.
    In: *IEEE international conference on robotics and automation
    (ICRA)*, Rome, Italy, April 2007, pp. 4975–4980.
Xia Y and Whitesides GM (1998) Soft lithography. *Annual
    Review of Material Science* 28: 153–184.
Yeom SW and Oh IK (2009) A biomimetic jellyfish robot based
    on ionic polymer metal comoposite actuators. *Smart Materials
    and Structures* 18(8): 085002.
Yoshizawa H, Chen YL and Israelachvili J (1993) Fundamen-
    tal mechanisms of interfacial friction. 1. Relation between
    adhesion and friction. *Journal of Physical Chemistry*. 97:
    4128–4140.

Appendix A

The vertical deflection $y_i(s)$ along each segment is the solu-
tion to the balance equation $d^4 y_i / ds^4 = w/D_i$, where w is
the gravitational load (units = N/m). The balance equation
has the general solution

$$y_i = \frac{ws^4}{24D_i} + \frac{a_i s^3}{6} + \frac{b_i s^2}{2} + c_i s + d_i. \qquad (11)$$

Here $a_i, b_i, c_i,$ and d_i are constants of integration that are
determined by solving a system of boundary conditions.
Each of these sets of boundary conditions correspond to the
six contact modes presented in Figure 6.

At the start of each time step (when the values for p_i are
updated), the constants in equation (8) are evaluated for the
following boundary conditions

$$y_1(0) = y_3(L) = 0$$
$$y_1(L_1) = y_2(L_1)$$
$$y_2(L_1 + L_2) = y_3(L_1 + L_2),$$
$$y_1(L_1) = y_2(L_1)$$
$$y_2(L_1 + L_2) = y_3(L_1 + L_2)$$
$$y_1(0) = \kappa_1$$
$$y_3(L) = \kappa_3$$
$$D_1\{y_1(L_1) \quad \kappa_1\} = D_2\{y_2(L_1) \quad \kappa_2\}$$
$$D_2\{y_2(L_1 + L_2) \quad \kappa_2\} = D_3\{y_3(L_1 + L_2) \quad \kappa_3\}$$
$$D_1 y_1(L_1) = D_2 y_2(L_1)$$
$$D_2 y_2(L_1 + L_2) = D_3 y_3 L_1 + L_2).$$

The solutions $\{a_i, b_i, c_i, d_i\}$ are then substituted back into
equation (8) in order to obtain expressions for y_i. If the seg-
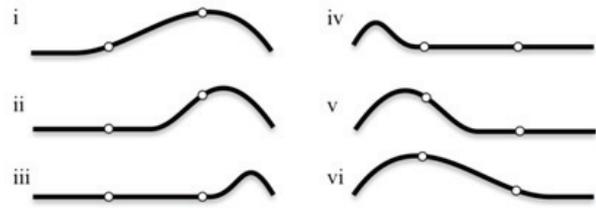ments deflect *away* from the surface at the two ends (i.e.

Fig. 6. Illustration of six contact modes in which at least one
segment is engaged in side contact. Each mode corresponds to a
unique set of boundary conditions.

$y_1(0) > 0$ and $y_3(L) < 0$), then the robot only makes tip
contact with the surface. Otherwise, the robot will engage in
one of the contact modes presented in Figure 6. We assume
that if $y_1(0) < 0$ and $|y_1(0)| > |y_3(L)|$, then the robot is
engaged in modes *i*, *ii*, or *iii*. If, instead, $y_3(L) > 0$ and
$|y_1(0)| < |y_3(L)|$, then the robot is engaged in modes
iv, *v*, or *vi*. The mode of contact (*i–vi*) is determined by
examining each mode separately with the aid of Maple 13
(Waterloo Maple Inc.):

(i)   The constants of integration $\{a_i, b_i, c_i, d_i\}$ and the
        edge of side contact ξ are determined by solving
        the 12 boundary conditions in equation (4) but with
        $y_1(0) = 0$ and $y_1(0) = \kappa_1$ replaced by $y_1(\xi) = 0$ and
        $y_1(\xi) = \kappa_1$, and adding the thirteenth boundary con-
        dition $y_1(\xi) = 0$. This mode occurs if the solution for
        ξ is positive and less than L_1.

(ii)   Solve $\{a_2, b_2, c_2, d_2, a_3, b_3, c_3, d_3, \xi\}$ for the boundary
        conditions $y_2(\xi) = y_3(L) = 0$, $y_2(L_1 + L_2) = y_3(L_1 +
        L_2)$, $y_2(\xi) = 0$, $y_2(L_1 + L_2) = y_3(L_1 + L_2)$, $y_2(\xi) =
        \kappa_2$, $y_3(L) = \kappa_3$, $D_2\{y_2(L_1 + L_2) \quad \kappa_2\} = D_3\{y_3(L_1 +
        L_2) \quad \kappa_3\}$, $D_2 y_2 (L_1 + L_2) = D_3 y_3 (L_1 + L_2)$. This mode
        occurs if the solution for ξ is between L_1 and $L_1 + L_2$.

(iii)   Solve $\{a_3, b_3, c_3, d_3, \xi\}$ for $y_3(\xi) = y_3(L) = y_3
        (\xi) = 0$ and $y_3(\xi) = y_3(L) = \kappa_3$. This mode occurs if
        $L_1 + L_2 < \xi < L$.

(iv)   Solve $\{a_1, b_1, c_1, d_1, \xi\}$ for $y_1(0) = y_1(\xi) = y_1
        (\xi) = 0$ and $y_1(0) = y_1(\xi) = \kappa_1$. This mode occurs
        if $0 < \xi < L_1$.

(v)   Solve $\{a_1, b_1, c_1, d_1, a_2, b_2, c_2, d_2, \xi\}$ for $y_1(0) =
        y_2(\xi) = 0$, $y_1(L_1) = y_2(L_1)$, $y_2(\xi) = 0$, $y_1(L_1) =
        y_2(L_1)$, $y_1(0) = \kappa_1$, $y_2(\xi) = \kappa_2$, $D_1\{y_1(L_1) \quad \kappa_2\} =
        D_2\{y_2(L_1) \quad \kappa_2\}$, $D_1 y_1 (L_1) = D_2 y_2 (L_1)$. This mode
        occurs if $L_1 < \xi < L_1 + L_2$.

(vi)   Solve $\{a_i, b_i, c_i, d_i\}$ and ξ for the boundary conditions
        in equation (4) but with $y_3(L) = 0$ and $y_3(L) = \kappa_1$
        replaced by $y_3(\xi) = 0$ and $y_3(\xi) = \kappa_3$, and adding the
        thirteenth boundary condition $y_3(\xi) = 0$. This mode
        occurs if the solution for ξ is between $L_1 + L_2$ and L

For sets of modes $\{i, ii, iii\}$ and $\{iv, v, vi\}$, the lengths of side
contact are defined as $\lambda = \xi$ and $\lambda = L \quad \xi$, respec-
tively. Once the mode shape and the expressions for y_i are
obtained, the global motion of the robot may be determined
by evaluating the horizontal distance Λ between the two
ends.